

RESEARCH ARTICLE

10.1002/2013JE004421

Key Points:

- How well do we know the polar hydrogen distribution

Correspondence to:

L. F. A. Teodoro,
luis.f.teodoro@nasa.gov

Citation:

Teodoro, L. F. A., V. R. Eke, R. C. Elphic, W. C. Feldman, and D. J. Lawrence (2014), How well do we know the polar hydrogen distribution on the Moon?, *J. Geophys. Res. Planets*, 119, 574–593, doi:10.1002/2013JE004421.

Received 29 APR 2013

Accepted 13 NOV 2013

Accepted article online 6 DEC 2013

Published online 18 MAR 2014

How well do we know the polar hydrogen distribution on the Moon?

L. F. A. Teodoro¹, V. R. Eke², R. C. Elphic³, W. C. Feldman⁴, and D. J. Lawrence⁵

¹BAER, NASA Ames Research Center, Moffett Field, Mountain View, California, USA, ²Institute for Computational Cosmology, Department of Physics, Durham University, Durham, U. K., ³Planetary Systems Branch, Space Sciences and Astrobiology Division, NASA Ames Research Center, Mountain View, California, USA, ⁴Planetary Science Institute, Tucson, Arizona, USA, ⁵Johns Hopkins University Applied Physics Laboratory, Laurel, Maryland, USA.

Abstract A detailed comparison is made of results from the Lunar Prospector Neutron Spectrometer (LPNS) and the Lunar Exploration Neutron Detector Collimated Sensors for Epithermal Neutrons (LEND CSETN). Using the autocorrelation function and power spectrum of the polar count rate maps produced by these experiments, it is shown that the LEND CSETN has a footprint that is at least as big as would be expected for an omnidirectional detector at an orbital altitude of 50 km. The collimated flux into the field of view of the collimator is negligible. A dip in the count rate in Shoemaker crater is found to be consistent with being a statistical fluctuation superimposed on a significant, larger-scale decrease in the count rate, providing no evidence for high spatial resolution of the LEND CSETN. The maps of lunar polar hydrogen with the highest contrast, i.e., spatial resolution, are those resulting from pixon image reconstructions of the LPNS data. These typically provide weight percentages of water-equivalent hydrogen that are accurate to 30% within the polar craters.

1. Introduction

The presence and distribution of hydrogen near the lunar surface is a matter of considerable interest [Watson *et al.*, 1961; Arnold, 1979]. This ancient surface, like that of Mercury, contains a record of the history of the inner solar system, and the likely association of hydrogen with water molecules can provide insights into the delivery and retention of volatile molecules over the past few billion years [Lawrence *et al.*, 2013; Paige *et al.*, 2013; Neumann *et al.*, 2013].

Remote sensing of the epithermal neutron flux coming from the lunar surface provides a measure of the hydrogen abundance in the top meter or so of the lunar regolith [Lingenfelter *et al.*, 1961; Metzger and Drake, 1990; Feldman *et al.*, 1991]. Cosmic rays interacting with nuclei in the regolith create energetic, fast neutrons that subsequently lose energy through inelastic and elastic collisions with other nuclei. Some of these neutrons escape into space before losing enough energy to be reabsorbed into another nucleus and this leakage flux contains information about the nuclear content of the upper regolith. Hydrogen provides a very effective moderator of intermediate energy, epithermal neutrons that predominantly lose energy through elastic scattering. Consequently, the presence of hydrogen in the top meter of regolith leads to a relatively low flux of epithermal neutrons leaking from the surface.

Pioneering work in this subject was performed by those working with the Lunar Prospector Neutron Spectrometer (LPNS) who mapped the lunar neutron flux at fast, epithermal, and thermal energies [Feldman *et al.*, 1998a; Elphic *et al.*, 1998; Feldman *et al.*, 1998b]. Fast neutrons provide a map of the mean atomic mass [Gasnault *et al.*, 2001], while thermal neutrons identify regions with higher abundances of neutron-absorbing nuclei such as iron, titanium, gadolinium, and samarium. A deficit of epithermal neutrons is seen over the mare regions, because the lower energy epithermal neutrons are sensitive to the neutron-absorbing nuclei [Lawrence *et al.*, 2006]. While this is not important for the polar regions, which have feldspathic composition characteristic of the lunar highlands, when making a global hydrogen map, Feldman *et al.* [2000] introduced a quantity epi^* to correct for the effects of these nonhydrogen absorbers at low latitudes. Nearer the poles, the main aspect of composition driving the epithermal neutron count

rate is hydrogen and the LPNS results showed reduced polar epithermal neutron count rates, implying the presence of polar hydrogen.

With the ~ 45 km full width at half maximum (FWHM) footprint size of the omnidirectional LPNS [Maurice *et al.*, 2004] and the inevitable stochastic noise present in the data, it was difficult to determine if the dips in count rate were associated with the typically subfootprint-sized permanently shaded regions (PSRs) that might be expected to host water ice deposits. Consequently, pixon image reconstruction techniques [Pina and Puetter, 1993; Eke, 2001] were employed to enhance the information that could be extracted from the data. Using the method introduced in Elphic *et al.* [2007], Eke *et al.* [2009] were the first to show that the data favored a scenario where the hydrogen was, on average, concentrated into the PSRs. This analysis was improved using updated maps of the PSRs by Teodoro *et al.* [2010], whose maps were used in the targeting of the Lunar Crater Observation and Sensing Satellite in its successful bid to find water ice in the Cabeus crater [Colaprete *et al.*, 2010].

NASA's Lunar Precursor Robotic Program was intended to "pave the way for eventual permanent human presence on the Moon" [Chin *et al.*, 2007]. The first mission of this program was the Lunar Reconnaissance Orbiter (LRO), which employs "six individual instruments to produce accurate maps and high-resolution images of future landing sites, to assess potential lunar resources, and to characterize the radiation environment" [Chin *et al.*, 2007]. One of these instruments is the Lunar Exploration Neutron Detector (LEND), with a primary objective being to "determine hydrogen content of the subsurface at the polar regions with spatial resolution of 10 km and with sensitivity to concentration variations of 100 parts per million at the poles" [Chin *et al.*, 2007]. Rather than taking omnidirectional measurements and using software to enhance the resulting images, as was done with the LPNS, the LEND Collimated Sensors for Epithermal Neutrons (CSETN) represent an attempt at a hardware solution to the challenge of making sharper maps of the lunar epithermal neutron count rate. This was to be achieved using a two-layer collimator with an outer layer of polyethylene to moderate the neutrons and an inner layer of boron to absorb them [Mitrofanov *et al.*, 2008].

Prior to launch, there were studies anticipating how the LEND CSETN might perform. Lawrence *et al.* [2010] used Monte Carlo modeling and simple scaling arguments with observations from the LPNS to infer that the neutron count rate through the small field of view of the collimator was going to be a rather low 0.18 neutrons per second. However, this disagreed with the estimate from Mitrofanov *et al.* [2008], who predicted a value of 0.9 neutrons per second.

Analyses of orbital LEND CSETN data have resulted in discordant inferences concerning the behavior of the collimator. Mitrofanov *et al.* [2010] claimed that the LEND CSETN was receiving "about 1.9" collimated neutrons per second. On the basis of this interpretation, Mitrofanov *et al.* [2010] concluded that epithermal neutron suppressions, and by implication, enhanced hydrogen concentrations, were not spatially coincident with permanently shaded regions. In response, Lawrence *et al.* [2011] contended that the LEND CSETN count rate was dominated by an uncollimated high-energy epithermal neutron component. As a consequence, Lawrence *et al.* [2011] concluded that the LEND CSETN data did not support the polar hydrogen distributions inferred by Mitrofanov *et al.* [2010]. A more comprehensive likelihood analysis of the time series data was performed by Eke *et al.* [2012], who considered the three different components contributing to the LEND CSETN count rate: The lunar collimated component, the lunar uncollimated component, i.e., neutrons from outside the collimator field of view on the Moon that scatter off spacecraft material into the detector, and neutrons generated by cosmic rays striking spacecraft material itself. Taking into account the three different components contributing to the LEND CSETN count rate and how they should vary with longitude, latitude, and spacecraft altitude, Eke *et al.* [2012] showed that the collimated count rate represented less than about 10% of the lunar-derived neutrons, allowing for potential systematic uncertainties. The uncollimated lunar neutrons, which provide a spatially varying background, dominated the count rate from the Moon. However, more than half of the LEND CSETN count rate is derived from cosmic rays striking the spacecraft itself [Eke *et al.*, 2012], so fewer than 5% of the detected neutrons were actually lunar and collimated. Eke *et al.* [2012] determined that 1% is the most likely fraction of the detected neutrons that are lunar and collimated, meaning that the effective footprint of the LEND CSETN will be set by the uncollimated lunar background component and is likely to be at least ~ 50 km in size. Miller *et al.* [2012] also concluded that the comparison of the LPNS and LEND CSETN data sets suggested that an admixture of uncollimated lunar flux was consistent with the LEND CSETN data and that this would degrade the spatial resolution from that of the collimator field of view.

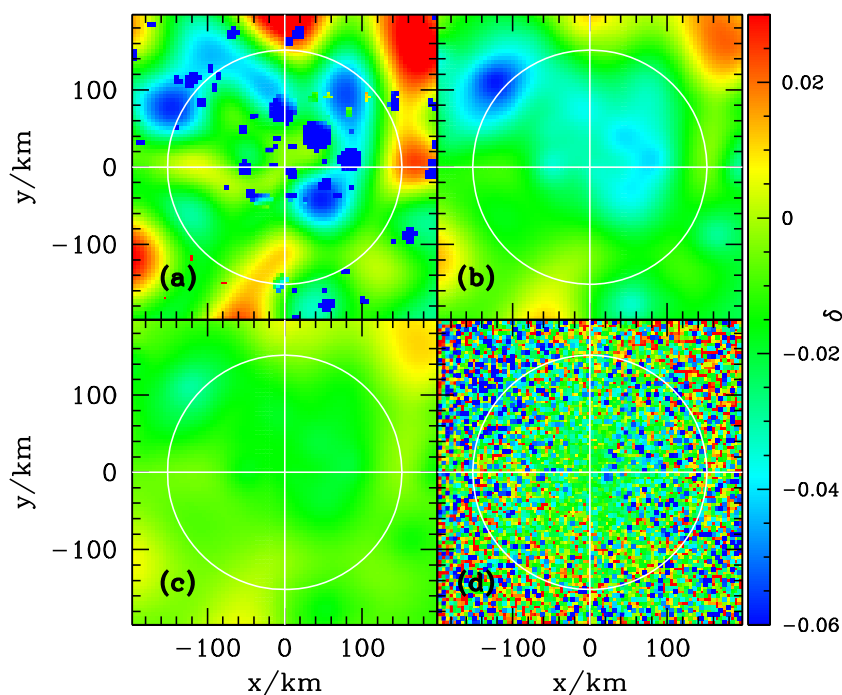


Figure 1. Maps illustrating the degradation of information during the process of making an observation. (a) Shows an example input map of fractional count rate difference, δ . (b) The map resulting from smoothing with the spatial response function of the LPNS at 30 km altitude. (c) Adding to the blurred map in Figure 1b, a uniform background with the same mean count rate as that in the input map leads to the results. (d) A noisy realization of the map shown in Figure 1c produces one which is what would be measured.

Recently, a number of papers have appeared [Litvak *et al.*, 2012a; Sanin *et al.*, 2012; Mitrofanov *et al.*, 2012; Litvak *et al.*, 2012b; Boynton *et al.*, 2012] that contain assertions to the effect that the LEND CSETN is producing a map with 10 km spatial resolution. Given the importance for the planning of future missions, it is imperative that the performance of the LEND CSETN is clarified for decision-makers outside the field of planetary neutron studies. The purpose of this paper is to determine empirically the instrumental spatial resolution and the background contamination in the data and hence the ability to map hydrogen near the lunar poles of the LEND CSETN. This will be achieved using techniques that are new to planetary neutron spectroscopy, but well-established in other scientific fields.

In the next section, two statistical measures will be introduced to characterize the performance of a detector given the output map it produces. These will then be applied in section 3 to the data sets from both the LPNS and LEND CSETN in order to compare the relative performance of these two detectors. The various arguments put forward by authors in support of statements about the proper functioning of the LEND CSETN are investigated in detail in section 4. The results from this study are discussed in section 5 and conclusions drawn in section 6.

2. Characterizing Detector Performance

There are three important ways in which measured maps of epithermal neutron count rate will be degraded representations of what actually leaves the lunar surface. A detector orbiting above the Moon does not solely receive neutrons from directly beneath it. Omnidirectional detectors count neutrons coming from all parts of the Moon out to the horizon, whereas an ideal collimated detector would have a restricted, but still extended, field of view. In both cases, the measured epithermal neutron map will be blurred by the extended spatial response function, or footprint, of the detector. This blurred map is further degraded with the inclusion of a uniform background due to neutrons produced by cosmic rays striking the spacecraft. These neutrons have nothing to do with the lunar surface composition and provide a uniform spatial background that dilutes any variations from lunar composition that may have been present. Finally, because the

detector counts neutrons, the measured map will be a noisy realization where the total counts in each pixel are drawn from a Poisson distribution with a mean taken from the appropriately blurred and diluted map.

Figure 1 provides an illustration of the impact of these effects for a hypothetical detector. Rather than showing a count rate map, these maps show the fractional difference

$$\delta(\mathbf{x}) = \frac{c(\mathbf{x}) - \bar{c}}{\bar{c}}, \quad (1)$$

where $c(\mathbf{x})$ is the count rate in the two-dimensional map at position \mathbf{x} and \bar{c} represents the mean count rate per pixel in the region $|x|, |y| < 600$ km. A distance of 600 km corresponds to almost 20° of latitude. This statistic is invariant under changes in detector efficiency or cosmic ray flux and thus represents a convenient way to compare detectors.

Figure 1a is the input map, which for illustrative purposes, is taken to be the pixon reconstruction of the LPNS data in the south polar region [Teodoro *et al.*, 2010]. The south pole is at the center of the image, radial distances from the pole are preserved and the zero of longitude is at the top of the figure. Blurring the map in Figure 1a with the spatial response of the LPNS at an altitude of 30 km leads to the map in Figure 1b. Small features are lost, while the larger features from the input map remain visible. Diluting the map in Figure 1b with a uniform spatial background having a mean count rate equal to that in the input map leads to the map shown in Figure 1c. This size of background from spacecraft-derived neutrons is more appropriate [Mitrofanov *et al.*, 2011; Eke *et al.*, 2012] for the LEND CSETN than the LPNS [Maurice *et al.*, 2004] because, while the LPNS was on a boom 2.5 m away from the main body of a relatively small spacecraft, the LEND is right next to the much more massive LRO. This uniform background is distinct from the background due to the uncollimated lunar neutrons that are scattered off of spacecraft material into the LEND CSETN detector and provide a spatially varying background.

The final aspect of the measurement procedure that acts to obscure the underlying lunar signal is the fact that integration times are finite, leading to inevitable stochastic noise in the collected data. Figure 1d shows a particular sampling of the map shown in Figure 1c, where the observation time map is like that of the LPNS during its low-altitude orbit. The fact that pixels near to the pole receive more visits and suffer less statistical noise is clearly visible in this map.

It is evident from Figure 1 that all three of these aspects of detector performance leave strong imprints on the measured data set. Thus, determining the relative merits of the LPNS and LEND CSETN boils down to choosing appropriate statistical measures that are sensitive to each of these contributing factors. In this way, the size of the instrumental spatial footprint, the background contamination, and the statistical noise can be estimated empirically from the maps constructed using data from these two experiments.

Two powerful statistical measures that are widely used in many different scientific disciplines to quantify the properties of continuous stochastic fields such as $\delta(\mathbf{x})$, are the *power spectrum* and the *autocorrelation function* [Peebles, 1980; Monin *et al.*, 2007]. Both of these quantities encode information about the amount of structure contained in a map on a variety of different spatial scales. In the field of space science, these statistical measures have been used in studies of the lunar gravitational potential [Wieczorek and Phillips, 1998], modeling of Martian dunes dynamics [Narteau *et al.*, 2009], helioseismology [Christensen-Dalsgaard *et al.*, 1985], X-ray variability from black hole accretion discs [McHardy *et al.*, 2006], galaxy clustering [Cole *et al.*, 2005; Eisenstein *et al.*, 2005], and the cosmic microwave background [Planck Collaboration, 2013] to name a few examples.

2.1. The Autocorrelation Function

The autocorrelation function of a map is a measure of the similarity between values in pixels at different relative positions. It is defined by

$$\xi(r) \equiv \langle \delta(\mathbf{x}) \delta(\mathbf{x} + \mathbf{r}) \rangle. \quad (2)$$

In this expression, \mathbf{r} represents a two-dimensional vector displacement in the two-dimensional map, the separation $r = |\mathbf{r}|$ and the average is over all pairs of pixels with separation r . See Appendix 1 and Figure A1 for further details. One needs to invoke the Ergodic Theorem to show that “average in space” is equivalent to “average over realizations” [Adler, 1981]. Isotropy guarantees that $\xi(r)$ is independent of the direction of the separation of the pixels. One can think of $\xi(r)$ as the mean product of pixel contrasts for pixels separated

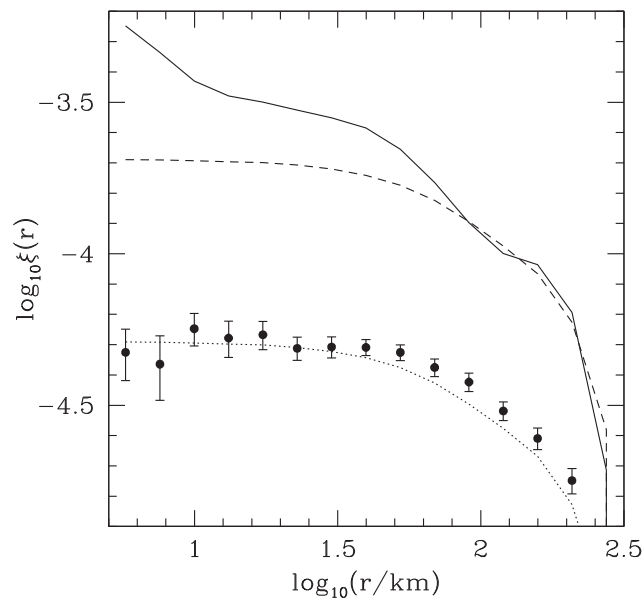


Figure 2. The impact of the measurement process on the autocorrelation function of polar neutron maps. Curves show the autocorrelation functions for the input map (solid), the blurred map without any uniform background included (dashed), and after a uniform background has been added (dotted). These correspond to Figures 1a, 1b, and 1c). Filled circles represent the autocorrelation function measured from the particular noisy realization shown in Figure 1d, with error bars representing the uncertainty due to sample variance, inferred using many different noisy realizations.

of the smoothed and unsmoothed maps coincide within the measurement error. This is illustrated in Figure 2, where the solid and dashed lines represent $\xi(r)$ for the unsmoothed and smoothed maps shown in Figures 1a and 1b, respectively. The smoothing kernel used was

$$W(r) = \frac{A}{(1 + (r/\sigma)^2)^2}, \quad (5)$$

with $\sigma = 35$ km to mimic the omnidirectional LPNS at 30 km altitude and A being a normalization constant [Maurice et al., 2004]. These autocorrelation functions have been calculated for polar data on the projection grid going out to $|x|, |y| = 600$ km from the south pole in 5 km square pixels (Figure 1 shows the central ninth of this region). In order to speed up the computation, fast Fourier Transforms were used in the computation and sufficient zero padding was included around the data region to prevent pixel pairs from periodic replicas contributing to $\xi(r)$. The results were identical to those calculated in the pixel domain, and very similar to those determined in the pixel domain when defining r to be the arclength on a spherical surface rather than the two-dimensional distance in the projection used in Figure 1.

The dotted line in Figure 2 represents the effect of a uniform background with a count rate equal to that of the mean lunar signal in the polar region being used for the calculation of the autocorrelation function. This amount of background is far larger than was suffered by the LPNS, but almost matches that experienced by the LEND CSETN. The fluctuations in the smoothed map become diluted by a factor of 2, meaning that the autocorrelation function is suppressed on all scales by a factor of 4. Figure 1c shows the associated loss of contrast in the map. $\xi(r)$ for the noisy map in Figure 1d is represented by the points in Figure 2. As the noise is assumed to be spatially uncorrelated, only the value of ξ at zero separation (not shown on this log plot) is systematically changed by the presence of noise. The larger separation values merely have statistical noise added to them. These are represented by the error bars, which are determined from the scatter between the individual measurements when many different noisy realizations of the same underlying map are made.

2.2. The Power Spectrum

The power spectrum is just the Fourier transform of the autocorrelation function and represents an alternative way of showing which spatial scales contain information. In terms of the wave number $\mathbf{k} = 2\pi/\lambda$, where

by a distance r . This function depends not only on the intrinsic clustering properties of the fractional count rate differences, but also on both the smoothing length imposed on the data by the instrumental spatial resolution and the amount of uniform background that is introduced.

In formal terms, smoothing can be represented by the convolution

$$\delta_s(\mathbf{x}) = \int_{\text{over all space}} \delta(\mathbf{x}') W(\mathbf{x} - \mathbf{x}') d^2\mathbf{x}', \quad (3)$$

where the smoothing kernel is normalized such that

$$\int W(\mathbf{x} - \mathbf{x}') d^2\mathbf{r} = 1, \quad (4)$$

and $\delta_s(\mathbf{x})$ represents the raw count rate map that has been smoothed by the spatial footprint of the detector. Qualitatively, on scales smaller than the size of the kernel, the correlation function will be approximately flat. For scales larger than a few smoothing lengths, the correlation functions

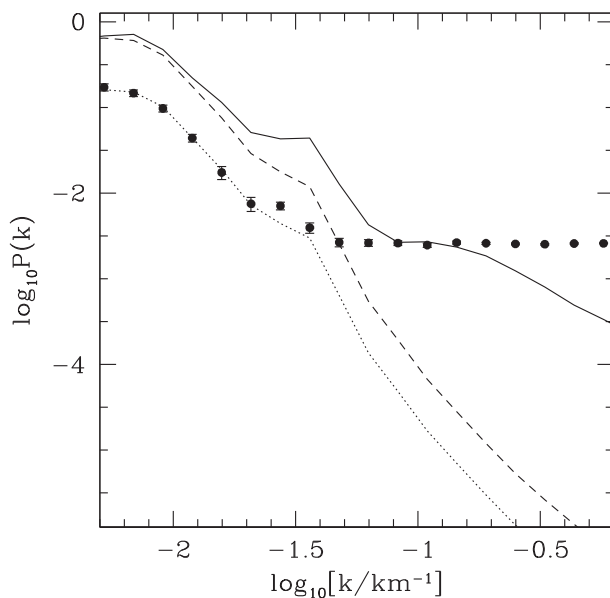


Figure 3. The impact of the measurement process on the power spectrum, shown as a function of wave number k in km^{-1} , of polar neutron maps. Solid, dashed and dotted lines show the power spectra for the input map and blurred maps, with and without a uniform background added, respectively. Filled circles represent the power spectrum of the particular noisy realization shown in panel Figure 1d, with error bars representing the uncertainty due to sample variance, inferred using many different noisy realizations.

the autocorrelation function at zero separation. However, this delta function contribution to $\xi(r)$ in pixel space transforms to a constant in wave number space. Thus, at small scales (large k) where the noise overwhelms what remains of the fluctuations in fractional count rate difference, the power spectrum goes flat, identifying precisely the mean level of statistical noise in the map.

The maps from the LPNS or LEND CSETN data sets result from a statistical sampling of the blurred, diluted input map that reflects the hydrogen distribution in the lunar regolith. Both the autocorrelation function and power spectrum of the resulting maps will provide complementary and comprehensive views of the impact that these detectors have had on the intrinsic lunar count rate map. In the following section, these two statistical estimators will be employed to quantify the performance of the LPNS and LEND CSETN instruments and hence infer how well we know the lunar hydrogen distribution.

3. Results for Lunar Neutron Data Sets

Data from the Geosciences Node of NASA's Planetary Data System (PDS) (<http://pds-geosciences.wustl.edu>) were used to create epithermal neutron maps from both the LPNS and LEND CSETN experiments. The time series Reduced Data Records up to 24 May 2011 for the LEND CSETN were processed almost as described by Boynton *et al.* [2012], with a few notable exceptions. Table 2 of that paper describes the impact that the various cuts on the data have for the number of one-second data records that form part of the analysis. However, the quoted number of total raw records (~ 59.6 million) exceeds the number of seconds during the claimed period (~ 56 million). Thus, at the first stage in the data reduction process, it is impossible to replicate the results of Boynton *et al.* [2012], precluding a more detailed comparison with that study. A couple of other differences in the reduction procedure adopted here are that an extra factor of $A_{i,j}$ has been included on the denominator of both equations (2) and (7) in Boynton *et al.* [2012], $A_{i,j}$ being the count rate normalization of the i th sensor during the j th switch-on period. Without this extra factor, the equations given in Boynton *et al.* [2012] are dimensionally incorrect. One additional important part of the Boynton *et al.* [2012] data reduction procedure, not detailed in that paper, is how variances are calculated for time series records where a subset of the four sensors are working and they happen to record zero counts. Equation (9) of

λ represents the corresponding wavelength in two-dimensional pixel space, the power spectrum can also be written as

$$P(k = |\mathbf{k}|) \equiv \langle |\delta_{\mathbf{k}}|^2 \rangle, \quad (6)$$

with $\delta_{\mathbf{k}}$ representing the amplitude of the k th mode in the Fourier decomposition of the map of $\delta(\mathbf{x})$ and the average is over modes with the same wave number k .

The power spectra for the four maps in Figure 1 are given in Figure 3. The removal of power at small scales resulting from blurring with the instrumental footprint manifests itself at large wave numbers. Once again the uniform background produces a scale-independent reduction of the power by a factor of 4.

The statistical noise (i.e., the difference between the expected and sampled contrasts in Figures 1c and 1d) in any pixel is assumed to be independent than that in other pixels.

Consequently, it only contributes to

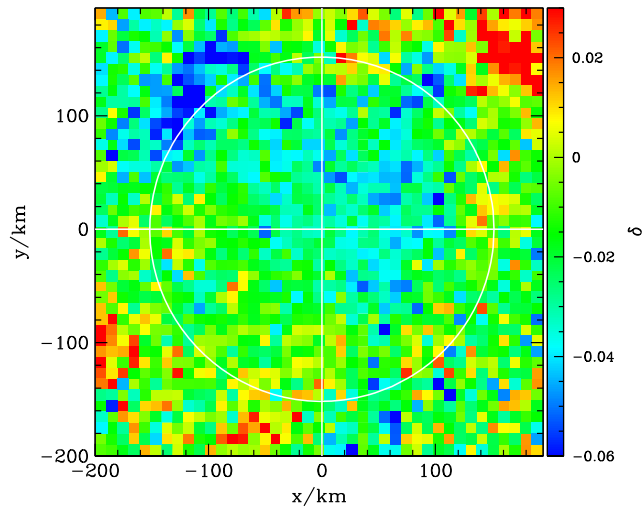


Figure 4. Map of the south pole LPNS fractional count rate difference using 10 km pixels and data from the 30 km orbital altitude period. The white circle represents a latitude of -85° . Statistical uncertainties on the values are ~ 0.01 at -88° , increasing to ~ 0.015 at -85° S. Note that the LPNS data from the PDS has had a small, 7% [Maurice *et al.*, 2004] uniform background component reintroduced for a like-with-like comparison with the LEND CSETN in Figure 5.

Boynton *et al.* [2012] appears to suggest that this involves the ratio $(0/0)^2$, which is not defined. In this paper, the following equation has been implemented to use individual sensor normalizations A_i^0 to convert the individual variances σ_{ij}^2 to that on the total “adjusted count rate” for observation j , R_j , via

$$\sigma_{R_j}^2 = \sum_{\text{on}} \sigma_{ij}^2 \left(\frac{\sum_{\text{all}} A_i^0}{\sum_{\text{on}} A_i^0} \right)^2. \tag{7}$$

The sums in this equation are over the relevant sets of sensors, i . Presumably, Boynton *et al.* [2012] performed a similar procedure. Other than these apparent modifications, the treatment of solar energetic particle events, outlier events, off-nadir measurements, instrumental warm-up, and cosmic ray variation has followed the procedure outlined by Boynton *et al.* [2012]. Reassuringly, all of the results and conclusions shown in this paper for the LEND CSETN data set do not change significantly when using either our

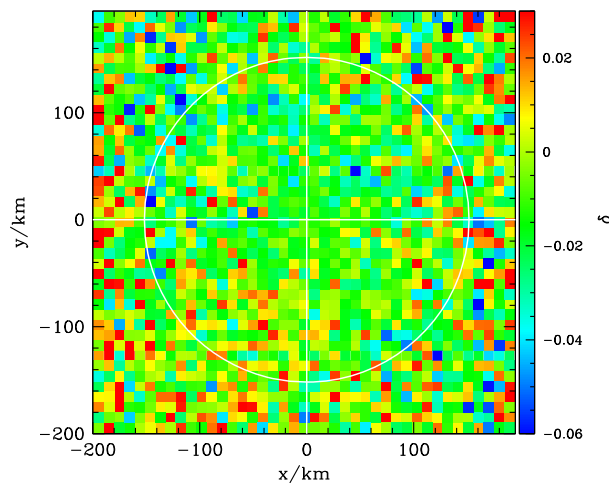


Figure 5. Map of the south pole LEND CSETN fractional count rate difference using 10 km pixels. The white circle represents a latitude of -85° . Statistical uncertainties on the values are ~ 0.01 at the pole, increasing to ~ 0.02 at -85° .

implementation of the data reduction procedure advocated by Boynton *et al.* [2012] or the alternative, independently developed analysis pipeline described by Eke *et al.* [2012].

Figures 4 and 5 show maps of the fractional count rate difference in the vicinity of the lunar south pole made using low-altitude LPNS epithermal neutron (7 months) and LEND CSETN (~ 21 months) data, respectively. It should be noted that the 7% uniform spacecraft background has been reintroduced into the LPNS map [Maurice *et al.*, 2004], whereas the reduced data on the PDS have had this background removed. This spacecraft background has been reintroduced in order that the *data* from the LPNS and LEND CSETN can be directly compared without needing to apply

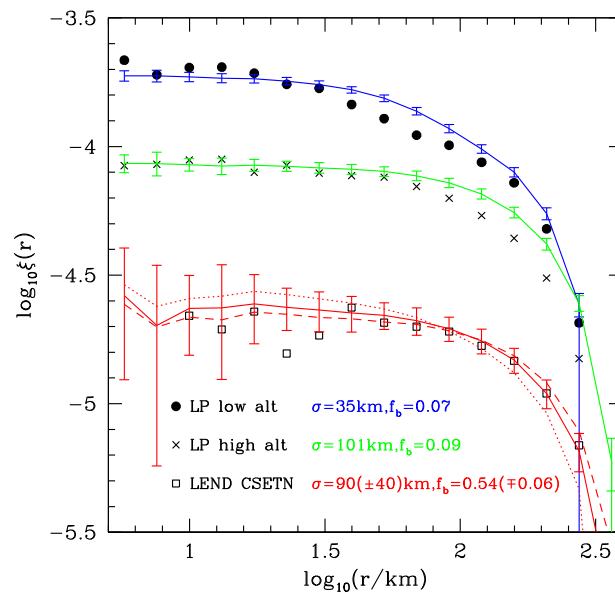


Figure 6. Autocorrelation functions for the different experiments. LPNS results for low and high altitudes are shown with black filled circles and crosses, respectively. The LEND CSETN results are shown with black open squares. The curves show the mean autocorrelation functions from 100 different realizations of the pixion reconstruction of the lunar south pole [Teodoro et al., 2010], and the error bars show the scatter among these realizations made using the sampling strategy for the appropriate detector. For the low-altitude LPNS mock observations, a smoothing kernel with $\sigma = 35$ km has been used (blue line). The green line assumes that $\sigma = 101$ km, as is appropriate for the high-altitude LPNS [Maurice et al., 2004]. The red solid line and error bars result from a detector with $\sigma = 90$ km for collecting lunar neutrons, and a uniform background fraction of $f_b = 0.54$. The dashed and dotted red lines were produced using ($\sigma = 130$ km, $f_b = 0.48$) and ($\sigma = 50$ km, $f_b = 0.60$), respectively.

the previous section to determine both the effective detector footprint sizes and the fractions of the counts that are in the form of a uniform spacecraft background.

Figure 6 shows the autocorrelation functions for the LPNS (also denoted by LP) data, from both high (100 km) and low (30 km) altitude periods and that from the LEND CSETN at its altitude of 50 km. Five kilometer square pixels in a region out to $|x|, |y| < 600$ km from the pole are used. This large area improves the statistical uncertainties, but the conclusions do not change when only the central ninth of that region (i.e., $|x|, |y| < 200$ km), shown in Figures 4 and 5 with 10 km square pixels, is chosen.

The data points in Figure 6 represent the autocorrelation functions for the south pole maps produced by the different detectors. The maps giving rise to these results are degraded versions of the epithermal neutron map that would have been created using a perfect detector with a delta function spatial response, no uniform background and no statistical noise. This “intrinsic” count rate map would contain bigger coherent fluctuations in contrast and therefore a larger autocorrelation function than any of those measured by the LPNS or LEND CSETN. Under the assumption that the different detectors are measuring the same intrinsic map, the measured autocorrelation functions of the maps constrain both the amount of blurring (i.e., the detector spatial resolution) and the uniform spacecraft background.

The curves in Figure 6 are constructed by assuming that the intrinsic map of the lunar south pole epithermal neutron count rate is that given by the pixion reconstructions of Teodoro et al. [2010]. As any higher-energy neutrons detected by the LEND CSETN reflect hydrogen variations in an almost identical way to the lower-energy epithermal neutrons measured by the LPNS [Lawrence et al., 2011], it is reasonable to use this map for modeling the polar data from the LEND CSETN. The intrinsic map is observed, by blurring with a footprint defined by σ , adding a uniform background, and including stochastic Poisson noise based upon the observation times in the different pixels for the different experiments. One hundred different random

model-dependent background corrections, because the inferred amount of spacecraft background into the LEND CSETN differs between studies (see Eke et al. [2012] for details). The pixels used are 10 km on a side and no other smoothing has been imposed on the data. The Cabeus region is clearly seen in the LPNS map as the area of relatively low count rate just over 5° from the pole centered around $(x, y) = (-120, 120)$ km. This is very much less pronounced in the LEND CSETN map, which does, however, have a single 10×10 km² pixel with count rate depressed by at least 6% in the Shoemaker Crater at position $(x, y) = (45, 45)$ km. The comparison between these two maps, made using the same data as were used by Boynton et al. [2012] in the same region with the same pixelation and the recommended data reduction procedures for the two different experiments, already makes clear that the LPNS produces a map with significantly more contrast than the LEND CSETN. Given the clear differences in the information contents present in the maps for the two different detectors, it is of interest to apply the statistical estimators described in

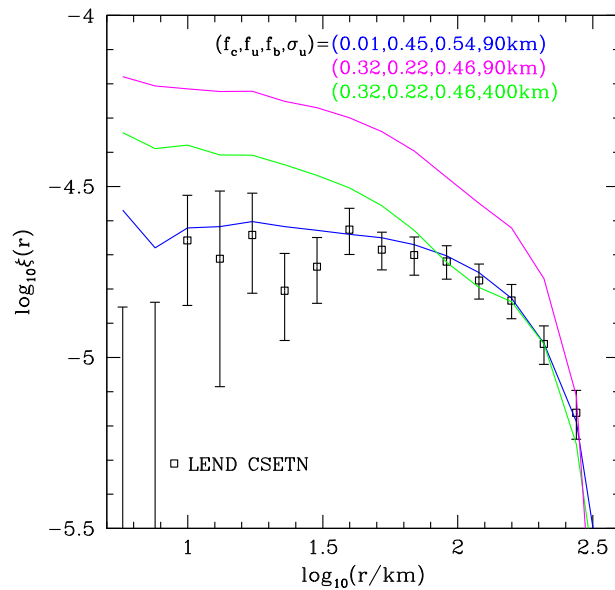


Figure 7. Observed autocorrelation function for the LEND CSETN (black open squares) with curves showing results from degrading the pixion south pole reconstruction with various types of detectors. The lines assume different count rate fractions in collimated lunar, f_c , uncollimated lunar, f_u , and uniform background spacecraft neutrons, f_b , as well as different detector footprint sizes for collecting the lunar uncollimated neutrons, parameterized with σ_u . For the blue line, $f_c = 0.01$, $f_u = 0.45$, $f_b = 0.54$, and $\sigma_u = 90$ km. Magenta shows $f_c = 0.32$, $f_u = 0.22$, $f_b = 0.46$, and $\sigma_u = 90$ km. In green is the result for a model detector with $f_c = 0.32$, $f_u = 0.22$, $f_b = 0.46$, and $\sigma_u = 400$ km.

the spatial resolution for the detected lunar neutrons. Also shown are model curves for which ($\sigma = 130$ km, $f_b = 0.48$) and ($\sigma = 50$ km, $f_b = 0.60$). At this level it is possible to trade off increasing the detector FWHM against decreasing the fraction of counts in the uniform spacecraft background, or decreasing the detector FWHM while increasing the diluting background fraction. Smaller assumed FWHM produce steeper autocorrelation functions that require a more uniform background to be added in order to fit $\xi(r)$ at small separations. Even so, the ($\sigma = 50$ km, $f_b = 0.60$) case, shown with the dotted line, is still too steep to match the data. In contrast, increasing the assumed FWHM wipes out more small-scale contrasts and produces an autocorrelation function that is flatter out to larger separations. Thus, a lower uniform background is necessary to degrade the intrinsic map enough to recover the LEND CSETN autocorrelation function. The case of ($\sigma = 130$ km, $f_b = 0.48$), shown with the dashed line in the figure, is still consistent with the data.

The autocorrelation functions in Figure 6 show that the effective spatial response to all lunar neutrons of the LEND CSETN needs to be characterized by $\sigma > 50$ km, with some degeneracy with the uniform background fraction. However, there exist testable hypotheses in the literature concerning the fraction of the detected neutrons that are of uniform spacecraft background [Mitrofanov et al., 2011; Eke et al., 2012]. These hypotheses also split the lunar component of the count rate into collimated and uncollimated parts, the former of which can be assumed to be collected with a FWHM of 10 km ($\sigma_c = 7.8$ km) set by the collimator field of view. The spatial response of this composite detector will be approximated with a neutron fraction-weighted sum of two smoothing kernels, $W(r)$ from equation (5). Mitrofanov et al. [2011] advocate the following fractions of neutrons coming from the lunar collimated, lunar uncollimated, and uniform spacecraft background components, respectively, ($f_c = 0.32$, $f_u = 0.22$, and $f_b = 0.46$). Eke et al. [2012] suggest that ($f_c = 0.01$, $f_u = 0.45$, and $f_b = 0.54$) better describes the LEND CSETN. The collimated component has a smoothing kernel width σ_c set so that the FWHM for this component is 10 km, and the uncollimated detector footprint is defined via σ_u .

Figure 7 shows the comparison of the autocorrelation function for the south pole map made with the LEND CSETN data and the results from various assumptions for how the detector performs. Provided that the uncollimated lunar neutrons are received with a wide footprint described by $\sigma_u = 90$ km, the component

noisy realizations are created and the mean of the results from these forms the curve. The error bars on the curves show the standard deviation individual realizations. The curves for LPNS assume $\sigma = 35$ km and 101 km for the low- and high-altitude cases, and that the uniform spacecraft background is 7% and 9%, respectively [Maurice et al., 2004]. That the observed map of the pixion reconstruction recovers the autocorrelation function of the low-altitude LPNS map is to be expected because these data and the blurring function and background were inputs in creating the pixion reconstruction. However, the autocorrelation function of the high-altitude LPNS data provides an independent check of the blurring and background reported by Maurice et al. [2004].

For the LEND CSETN case, the red solid curve in Figure 6 has degraded the intrinsic map with a uniform spacecraft background count rate fraction of $f_b = 0.54$ [Eke et al., 2012], and used $\sigma = 90$ km to describe

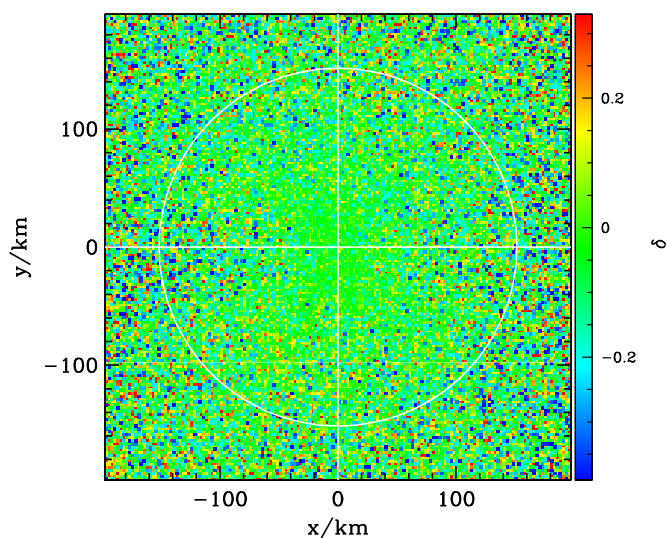


Figure 8. Map of the south pole LEND CSETN corrected fractional count rate difference using 2.5 km pixels. The correction assumes that a uniform spacecraft background of $f_b = 0.54$ was present in the data, so the corrected pixel δ values are $1/(1 - f_b)$ the size of the uncorrected ones. The white circle represents a latitude of -85° . Statistical uncertainties on the values are ~ 0.04 at the pole, increasing to ~ 0.08 at -85° .

fractions inferred by *Eke et al.* [2012] do degrade the pixon reconstruction to the extent that the resulting map has an autocorrelation function that is consistent with that determined from the LEND CSETN south pole map. Using $\sigma_u = 90$ km and the component fractions asserted by *Mitrofanov et al.* [2011] to degrade the pixon reconstruction produces a map that has a far more coherent structure than is present in the map from the LEND CSETN data. Even if the lunar uncollimated component is given an unrealistically broad spatial response with $\sigma_u = 400$ km, which implies that a significant fraction of these neutrons come from so far away that they originate off the lunar limb, the presence of a large collimated component still leads to too much small-scale coherent structure in the map to be consistent with the LEND CSETN data.

One might wonder if the model autocorrelation functions depend sensitively upon the use of the decoupled pixon reconstruction as the underlying map. They do not. Even with the unrealistically narrow composite LEND CSETN footprint advocated by *Mitrofanov et al.* [2011], the blurring with the power spectrum function leads to a very similar $\xi(r)$ to that found when the intrinsically smoother, coupled pixon reconstruction is used.

One might also wonder if the use of 10 km pixels prevents the true capabilities of the LEND CSETN from being seen in this analysis. Figure 8 shows the LEND CSETN south pole map sampled using 2.5 km pixels. The uniform spacecraft background has also been statistically removed, which acts to amplify the fluctuations by a factor of $1/(1 - f_b)$. Relative to Figure 5, the color scale has been expanded. The naive optimist may think that this is necessary because the smaller pixels are allowing higher contrast features to be seen. In contrast, a realist might note that the fluctuations appear to be larger in regions that are less well-sampled, so one might reasonably expect that latitude-dependent statistical noise is largely responsible for the content of this map. These two possibilities are distinguishable using a technique such as the autocorrelation function.

Figure 9 shows uniform spacecraft background-corrected autocorrelation functions from the LEND CSETN and the LPNS at both high and low altitudes. A LEND CSETN spacecraft background of $f_b = 0.54$ has been assumed. This is the value determined by *Eke et al.* [2012], which is larger than the $f_b = 0.46$ advocated by *Mitrofanov et al.* [2011]. Had this latter uniform background been adopted, then the resulting corrected autocorrelation function would have been lower by almost 40%. Also shown with a line is the computed autocorrelation function for the LEND CSETN map computed using 2.5 km pixels. This is indistinguishable from that calculated from the 5 km pixel map. At separations of 10 – 100 km, the corrected LPNS low-altitude map shows significantly more coherent structures than the LEND CSETN, which yields similar results to the LPNS at an altitude of ~ 100 km. Using a longer period of time series data from the LEND CSETN would reduce the statistical uncertainties on the polar map and its autocorrelation function without systematically changing the autocorrelation function. Extra data will decrease neither the

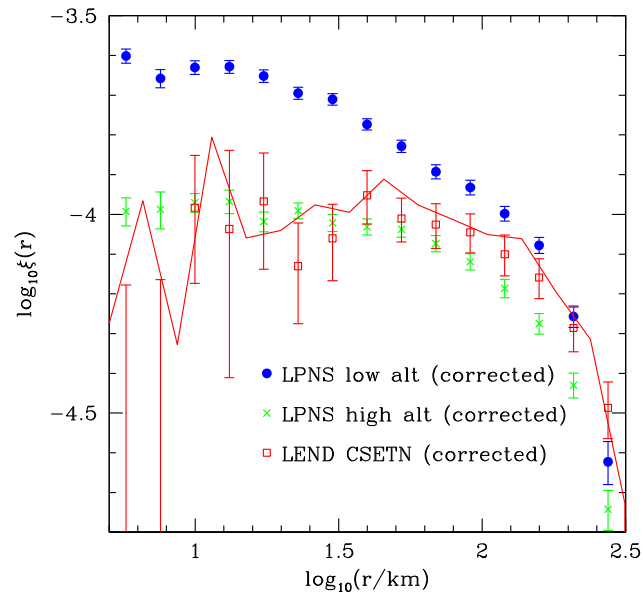


Figure 9. Autocorrelation functions for the spacecraft background-corrected south pole maps. The LPNS results are shown with filled blue circles and green crosses for low- and high-altitude maps, respectively. The LEND CSETN results, which are corrected assuming $f_b = 0.54$, are shown with open red squares. All points correspond to autocorrelation functions computed from maps made using 5 km pixels. The red line shows the effect of computing the autocorrelation function for the LEND CSETN map with 2.5 km pixels shown in Figure 8.

uniform spacecraft background contribution nor the broad LEND CSETN spatial response that wipes out small-scale coherent structures. These instrumental characteristics will not improve with time, and

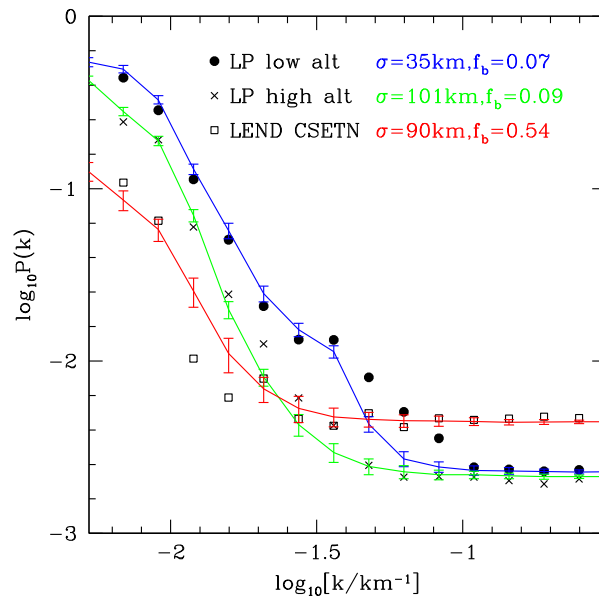


Figure 10. Power spectra as functions of wave number k in km^{-1} , with black symbols representing results from measurements of the south pole δ maps from the different experiments: filled circles (LP at low altitude), crosses (LP at high altitude), and open squares (LEND CSETN). The colored curves correspond to the power spectra from mock data sets made by observing the pixon reconstruction of Teodoro *et al.* [2010] assuming ($f_b = 0.07, \sigma = 35$ km) (blue), ($f_b = 0.07, \sigma = 101$ km) (green), and ($f_b = 0.54, \sigma = 90$ km) (red). These curves are appropriate for the LPNS at low altitude, LPNS at high altitude, and LEND CSETN, respectively.

their impact is clearly imprinted on the autocorrelation function of the derived maps presented here.

Figure 10 shows the corresponding power spectra for the data sets and model fits given in Figure 6. This makes clear that the noise level at small scales is higher for the LEND CSETN map than either the low- or high-altitude LPNS maps. The low-altitude LPNS data only becomes noise dominated for scales smaller than $\lambda \sim 2\pi/0.1 \sim 60$ km. For the high-altitude LPNS data, while the larger footprint suppresses power on intermediate scales relative to the low-altitude case, the noise level is similar for both data sets. The scale at which noise starts to dominate the power spectrum of the LEND CSETN map is nearer to $\log_{10} k = -1.6$ or $\lambda \sim 250$ km. Thus, independent of what the footprint of the LEND CSETN actually is, the contribution of noise is such that the LEND CSETN map only has useful information down to scales that are ~ 4 times as large as the resolution of the LPNS. The relative

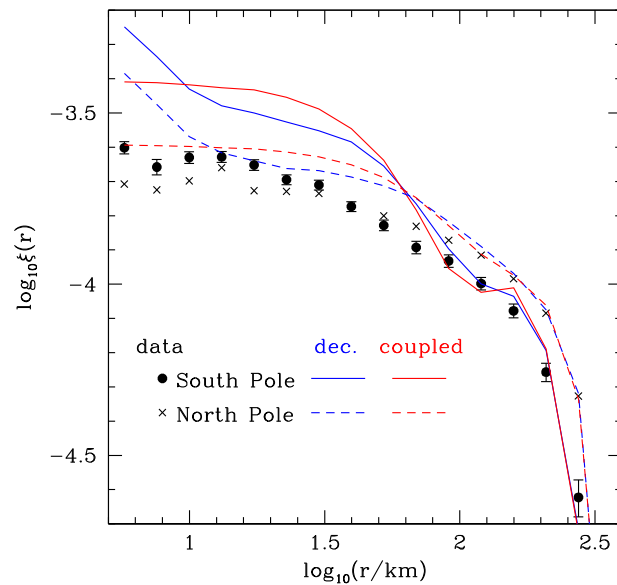


Figure 11. Autocorrelation functions for low-altitude north (crosses) and south (filled circles) pole LPNS data and their pixon reconstructions. Coupled (red) and decoupled (blue) reconstructions are shown for the south and north poles using solid and dashed lines, respectively.

component would be higher by a factor of $1/f_c \sim 100$, effectively washing out any fluctuations on all scales considered here. While longer integration times will reduce the noise level in the LEND CSETN map evident at large wave numbers in Figure 10, this will not systematically change the power on larger scales where the noise does not dominate. The LEND CSETN map, even adjusted for the uniform spacecraft background, will still remain a blurred version of the low-altitude LPNS map.

Having determined that the low-altitude LPNS represents the best data set for mapping the lunar hydrogen distribution, one can then ask, how do image reconstruction algorithms alter the accessible information from this data set, and address the question posed in the title of this paper. The points in Figure 11 show autocorrelation functions for both the north and south pole LPNS maps. There are interesting differences between the results from the north and south pole regions, with larger autocorrelations on 100 km scales in the north, while the south contains higher contrasts on scales below 30 km. This presumably reflects the different crater sizes and nature of the hydrogen distributions in these two regions.

Also shown with curves in Figure 11 are the autocorrelation functions of pixon reconstructions of the two polar regions. Image reconstruction methods are widely used and produce sharpened maps that, when blurred with the instrumental footprint, yield maps that are statistically indistinguishable from the observed map. For detectors with well-understood footprints, this enables extra information to be extracted from the data set. Both coupled and decoupled reconstructions [Elphic et al., 2007; Eke et al., 2009] are shown to amplify the autocorrelation functions significantly as a result of the enhanced contrasts on small scales. Even the coupled reconstructions of Eke et al. [2009], which did not allow the count rates in the cold traps to vary independently from those in nearby sunlit regions, thus leading to a smooth reconstruction, increase the correlation function by a factor of ~ 2 . The reconstructions that decoupled the cold trap pixels from the sunlit pixels, allowing larger contrasts to be found between cold trap and sunlit regions, show more power on scales less than ~ 10 km than the coupled reconstructions, but only by moving power from ~ 30 km scales. As shown by both Eke et al. [2009] and Teodoro et al. [2010], these decoupled reconstructions provided better fits to the residuals in the vicinity of cold traps, and thus represent the highest contrast, and hence spatial resolution, maps of the lunar polar hydrogen distribution that are currently available.

4. Other Evidence

The results in the previous section raises the question as to what is wrong with the arguments put forward by those advocating that the LEND CSETN is an effective collimated neutron detector. This section addresses these various claims in more detail.

noise levels of the LPNS and LEND CSETN data sets should not be a surprise, because the low-altitude LPNS received $c_{LP} \sim 21$ neutrons per second (including the uniform background) and operated for $t_{LP} \sim 7$ months, whereas the total LEND CSETN count rate is approximately $c_{LEND, CSETN} \sim 4$ neutrons per second and the data set being used is only about three times as lengthy, i.e., $t_{LEND, CSETN}/t_{LP} \sim 3$. Thus, one should expect the noise level to be higher by $c_{LP} t_{LP}/(c_{LEND, CSETN} t_{LEND, CSETN}) \sim 1.7$. This corresponds to the offset of $\log_{10}[1.7] \sim 0.24$ that is seen at large wave numbers. This noise level for the LEND CSETN is derived including both the uncollimated lunar and spacecraft background components in $c_{LEND} \sim 4$ per second. If these neutrons were not included, then the noise fluctuations in the lunar collimated

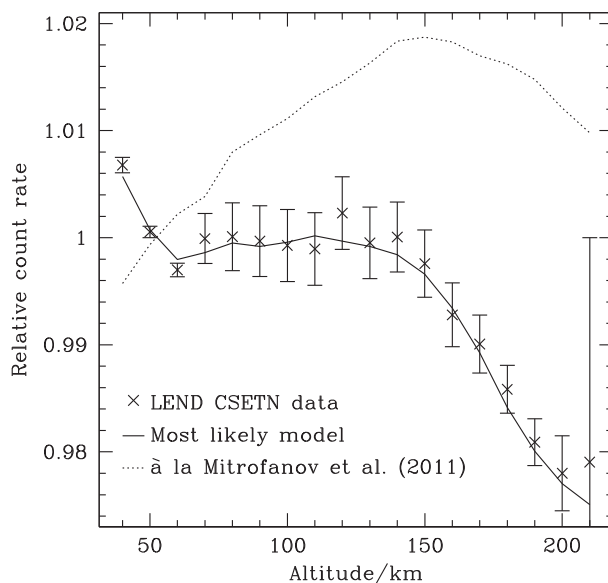


Figure 12. Variation of the count rate, relative to the mean throughout the time series, as a function of altitude. The crosses with error bars represent the LEND CSETN data, reduced as described by *Eke et al.* [2012], and the solid line shows the most likely model fit with collimated fraction, $f_c = 0$, a uniform background fraction of $f_b = 0.57$ and the remaining 0.43 in uncollimated lunar higher-energy neutrons. Component fractions as advocated by *Mitrofanov et al.* [2011] lead to the dotted line.

and the overall count rate decreases with increasing altitude of the detector, it is apparent that there must be a significant lunar uncollimated neutron component, as quantified by *Eke et al.* [2012].

The recent set of papers claiming that the LEND CSETN has a 10 km footprint do not explain the altitude dependence of the observed count rate. The nearest these authors come to discussing the altitude dependence is in *Litvak et al.* [2012b], who state that “Data from the commissioning orbit is the important part of the instrument in-flight calibration because it measured at the variable altitude above the Moon. ... In this paper we did not discuss these measurements in details and did not use it as part of the data reduction process.” In short, the commissioning data provide a valuable way to assess the performance of the LEND CSETN. Yet, neither *Litvak et al.* [2012b] nor any of the other papers in this set report any results from the commissioning orbit data.

Fortunately, the LEND CSETN commissioning phase data are now publicly available on the PDS and can be included into the likelihood analysis presented by *Eke et al.* [2012], who did not have access to them. The results of performing this experiment combining the 80 days of commissioning data with the mapping data from 15 September 2009 until the end of 2010, are shown in Figure 12. Count rates are divided by the mean over the whole time series to give the relative count rate as a function of altitude. Error bars are much larger for altitudes above 60 km, at which the detector was orbiting only during the short commissioning phase. A reanalysis of the time series in the manner of *Eke et al.* [2012], including the commissioning phase data, leads to most likely component fractions that are $f_c = 0.00$, $f_b = 0.57$ and an uncollimated lunar count rate comprising a fraction $f_u = 0.43$ of the total LEND CSETN count rate. These are very similar to those found by *Eke et al.* [2012], namely $f_c = 0.01$, $f_u = 0.455$, and $f_b = 0.535$. This model fits the data well over the range of altitudes. The fact that the data do not decrease in a monotonic fashion with altitude is a consequence of the fact that the elliptical commissioning orbit had a periapsis over the lunar south pole [*Litvak et al.*, 2012b] and intermediate altitudes were only attained over equatorial latitudes. This is where the iron-rich mare produces a higher flux of energetic neutrons, owing to the higher average atomic mass there. This effect in CSETN can be seen in Figure 10 of *Litvak et al.* [2012a]. Only the north pole is measured at altitudes of ~ 200 km, so it is a combination of the lower intrinsic count rate and the altitude dependence of the components that leads to the rapid drop off in count rate at high altitude. The dotted line shows the model with the count rate component fractions advocated by *Mitrofanov et al.* [2011]. For the high-

4.1. The Altitude Dependence of the LEND CSETN Data

One piece of evidence presented by *Eke et al.* [2012] that the lunar flux into the LEND CSETN was predominantly uncollimated, was the altitude dependence of the count rate. The three components contributing to the neutron count rate should have different variations with detector altitude. Spacecraft-generated neutrons increase in count rate as the detector moves away from the Moon and less cosmic ray shielding occurs. The collimated component should have a rate that is roughly independent of altitude, provided the collimator field of view remains filled by the lunar disc. In contrast, the count rate of uncollimated neutrons will decrease as the detector moves to higher altitudes and the Moon subtends a smaller solid angle. Given that the majority of detected neutrons in the LEND CSETN are generated from cosmic rays striking the spacecraft [*Eke et al.*, 2012]

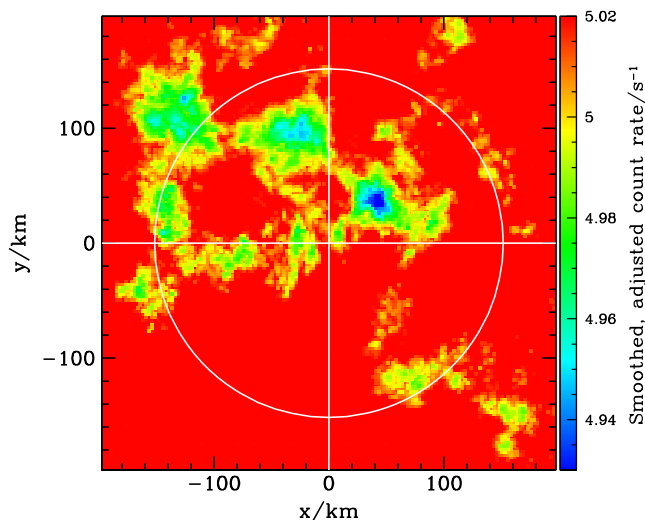


Figure 13. LEND CSETN smoothed, adjusted count rate map of the lunar south pole.

est altitudes, the decrease in count rate over the north pole is sufficiently strong that even this model with a large lunar collimated component produces a decrease of count rate with increasing altitude. However, when the relative count rate is fixed at 50 km, the component fractions advocated by *Mitrofanov et al.* [2011] are clearly ruled out by the data at all other altitudes. This result strongly reinforces those of section 3 and *Eke et al.* [2012] that the component fractions of *Mitrofanov et al.* [2011] are inconsistent with LEND CSETN collimated and background count rates.

4.2. Shoemaker Crater

Shoemaker Crater has a diameter of ~ 50 km and is located at a latitude of -88° . This crater covers just $\sim 0.02\%$ of the lunar surface, yet the arguments made by *Litvak et al.* [2012b] and *Boynton et al.* [2012] that the LEND CSETN is producing a high spatial resolution map rely strongly on data from this location.

Litvak et al. [2012b] argue that, using just over two years of data, the LEND CSETN provides a 4.6σ significance detection of a lower count rate in the Shoemaker Crater relative to the rest of the annulus at the same latitude, and imply that this provides evidence of the proper functioning of the collimator. Shoemaker Crater has a diameter of 50 km, whereas the rest of the annulus at -88° is ~ 300 km long and the collimator field of view is 10 km. Repeating the measurement using data from the omnidirectional LPNS reveals a $\sim 4\sigma$ count rate deficit using only seven months of low-altitude data. Given that the LPNS was an omnidirectional detector, this demonstrates that Shoemaker Crater is too large relative to the field of view of the LEND CSETN collimator for such a measurement to pertain to the effectiveness of the collimator.

The analysis of Shoemaker Crater by *Boynton et al.* [2012] claims that there is a significant and narrow dip in the measured count rate, which is much sharper than the broader dip present in the LPNS data. From the results in the previous section, where it was shown that the LPNS maps had much greater contrast than those from the LEND CSETN, even when the uniform background contribution was removed from the LEND CSETN map, one should immediately suspect that any sharp dips must be the result of stochastic noise. If the LEND CSETN did have resolution on 10 km scales, then the map it produced, after uniform background correction, would have a higher autocorrelation function on small scales than that from the LPNS, which is not the case.

To try and illustrate that the count rate dip in Shoemaker supports the claim that the LEND CSETN has a 10 km FWHM spatial resolution, *Boynton et al.* [2012] used a latitude-dependent box smoothing with a radius that is 10 km at the pole and already ~ 19 km at the latitude of Shoemaker. Adopting this same smoothing of the weighted, adjusted count rates for the LEND CSETN data reduced as described by *Boynton et al.* [2012] with the additional points noted in section 3, leads to the smoothed count rate distribution shown in Figure 13. The mean count rate in the region shown is 5.04 neutrons per second, so the color scale has been truncated at the high end to try and reproduce figure 7 in *Boynton et al.* [2012]. While Figure 13 is quite similar in appearance to figure 7 of *Boynton et al.* [2012], the depth of the depressions in count rate is only about

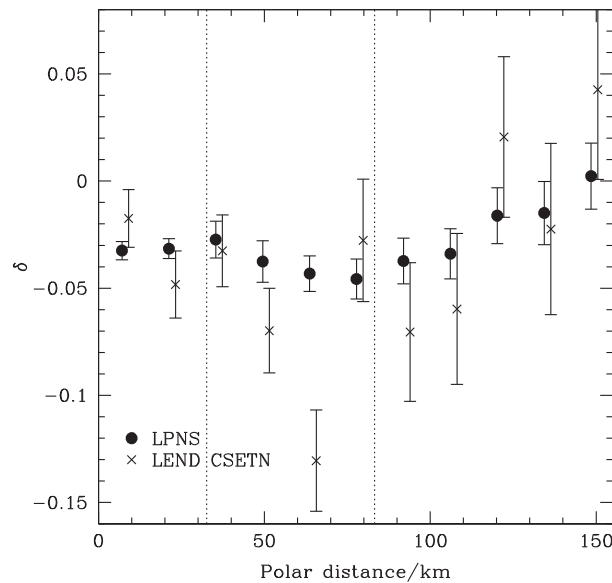


Figure 14. Fractional count rate difference as a function of distance from the south pole along longitude 45°, through Shoemaker Crater. The filled circles and crosses show results for the LPNS and LEND CSETN, respectively. Each data point corresponds to one of the 10 km pixels along $y = x$ in Figures 4 and 5. Uniform backgrounds of $f_b = 0.54$ and $f_b = 0.07$ for the LEND CSETN and LPNS, respectively, have been removed to enhance the contrasts. Error bars show the 1σ error on the mean δ in each pixel. The LEND CSETN results have been displaced by 2 km in polar distance for clarity. Vertical dotted lines delineate the limits of Shoemaker Crater.

CSETN contrast has been amplified by a factor $1/(1-f_b)$ to “correct” the dilution from the uniform spacecraft background. $f_b = 0.54$ has been used, which more than doubles the contrast evident in the uncorrected map. A value of $f_b = 0.07$ has been used to correct the LPNS data. The center of Shoemaker Crater lies ~ 60 km from the pole. One pixel, ~ 65 km from the pole, lies below the neighboring LEND CSETN pixel values, and a significant dip on 10 km scales would be indicative of a significant collimated component of the LEND CSETN count rate. Thus, the question is, how significantly far beneath the results for neighboring pixels does this one lie? The error bars shown on these points only represent the statistical uncertainties associated with the counting experiment and how they are altered by the various adjustment and correction factors applied through the data reduction procedure. They do not include inherent systematic uncertainties associated with the various corrections and should thus be viewed as appropriate for the case of zero systematic errors in the data reduction procedure. Under this assumption, the significance of the difference between two pixel values, $\delta_1 \pm \sigma_1$ and $\delta_2 \pm \sigma_2$ will be 5 standard deviations, where

$$S = \frac{|\delta_1 - \delta_2|}{\sqrt{\sigma_1^2 + \sigma_2^2}}. \quad (8)$$

Thus, the pixel at ~ 65 km is just under 2σ below that at 50 km and almost 2.8σ beneath that at 80 km from the pole. Given that, averaged over the entire polar region, the LEND CSETN is less able than the LPNS to detect fluctuations at small scales, as shown in the previous section, one may safely conclude that this particular low $10 \times 10 \text{ km}^2$ pixel is entirely consistent with being a statistical fluctuation.

The statistical fluctuation pushing this one pixel to a low count rate is superimposed on a broader region where $\delta < 0$, as evident from Figure 13. This is of no consequence to the argument concerning whether or not the LEND CSETN has a spatial resolution of 10 km. It merely shows that the LEND CSETN can detect large-scale features just as would be expected from an uncollimated high-energy epithermal neutron detector such as it is. If one were tempted to argue that 10 km pixels are too large to see the full capability of the

half that found by *Boynton et al.* [2012]. Why this is so is not clear. However, confidence in Figure 13 can be taken from the fact that it is very similar to the map found with the independent data reduction process used by *Eke et al.* [2012]. It is also consistent with the simple binning of the fractional count rate difference in Figure 5. While there is one pixel in that figure at (45, 45) km from the pole within Shoemaker having $\delta \sim -0.06$, averaging over the region corresponding to the box smoothing scale used for Figure 13 gives $\bar{\delta} \sim -0.026$. These δ values are measured relative to the mean count rate in a region extending 400 km from the pole, where $\bar{c} = 5.08$. Thus, $\bar{\delta} \sim -0.026$ corresponds to a count rate of ~ 4.94 neutrons per second, consistent with that found in Figure 13.

A trace of the fractional count rate difference as a function of distance from the lunar south pole along longitude 45° is shown in Figure 14. The LEND

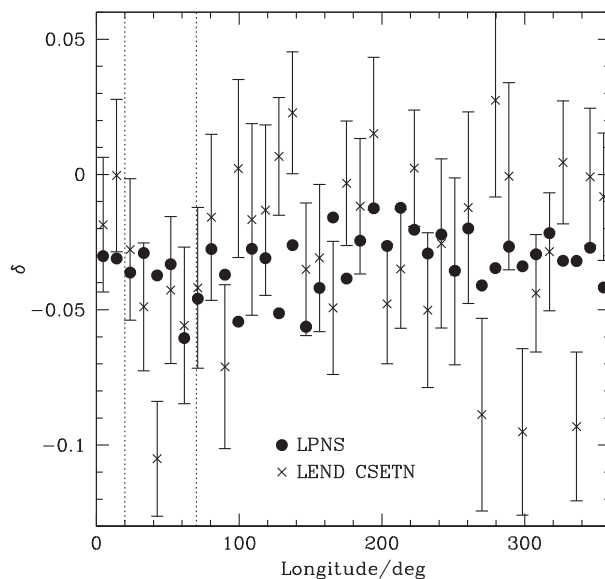


Figure 15. Fractional count rate difference as a function of longitude for a 10 km wide annulus at latitude -88° . Filled circles and crosses show results for the uniform background-corrected LPNS and LEND CSETN, respectively. Data points every ~ 10 km in azimuth are shown. Error bars on the LEND CSETN points show the 1σ error on the mean δ in each pixel. For clarity, the relatively small uncertainties ($\sim \pm 0.01$) on the LPNS results are not shown. Vertical dotted lines delineate the limits of Shoemaker Crater.

longitudes. The larger scatter in the LEND CSETN δ values, compared with those from the LPNS, is very clear. If these small-scale fluctuations represented real features on the lunar surface, then they would show up as coherent contributions to the autocorrelation function and power spectrum. They do not. Thus, it is appropriate to conclude that these small-scale fluctuations are the result of stochastic noise.

4.3. The Lunar Uncollimated Background

In order to produce maps of the collimated lunar component, *Boynton et al.* [2012], *Sanin et al.* [2012], and *Mitrofanov et al.* [2012] remove a component of uncollimated lunar background flux from the LEND CSETN count rate. Despite the choice of color scheme, figure 9 of *Boynton et al.* [2012] shows that the range of variation in combined background from the spacecraft and lunar uncollimated components amounts to no more than ~ 4 parts in 1000. This means that it is essentially spatially invariant near the pole, and any fluctuations seen in the total count rate map are ascribed to the lunar collimated component. This lack of variation in the lunar uncollimated component at the poles is inconsistent with that predicted by Monte Carlo neutron transport models [*Lawrence et al.*, 2011]. Furthermore, the low value of 1.1 counts per second assumed by *Boynton et al.* [2012] for the lunar uncollimated component would not be able to recreate the higher count rates seen over mare regions by the LEND CSETN [*Lawrence et al.*, 2011; *Eke et al.*, 2012].

Mitrofanov et al. [2012] adopt a slightly different approach that has a very similar effect. A “reference” map is made by smoothing the LEND CSETN data on a scale of ~ 230 km. The difference between this greatly smoothed map and one with a latitude-dependent smoothing radius of 11 km at the pole growing to 25 km at -70° latitude is used to determine where “local suppression/excess spots” exist. If the lunar uncollimated background results from neutrons coming from a scale of ~ 80 km across on the lunar surface, as one might anticipate for an omnidirectional detector at an altitude of 50 km, then this reference map will be too smooth to include any regional variations due to uncollimated lunar flux. Any such variations will then be ascribed to the collimated lunar component, which is anyway already smoothed on scales larger than the collimator field of view. There is no way that such an analysis can determine whether or not the LEND CSETN is behaving as a collimated detector.

Sanin et al. [2012] define their “local background” for a given crater using either a region at the same latitude or the LEND CSETN polar map smoothed on a similar large scale to *Mitrofanov et al.* [2012]. The similar-

LEND CSETN, then a glance at the autocorrelation results in section 3 should remove such a fanciful notion. The lack of coherent fluctuations relative to the LPNS results out to scales of ~ 100 km in the entirety of the LEND CSETN polar map demonstrates convincingly that statistical noise, not the resolution of underlying sharp features, is responsible for the variations on these pixel scales.

One further piece of evidence is shown in Figure 15, where a 10 km wide band around latitude -88° is presented for uniform background-corrected versions of both the LPNS and LEND CSETN data. The data points represent ~ 10 km long sections of the annulus, chosen because this is the field of view of the LEND CSETN collimator. Shoemaker Crater is situated at longitude 45° , where a single insignificantly lower pixel can be seen for the LEND CSETN. Comparably low values of δ are seen in three other pixels at higher lon-

ity between figure 1 in *Sanin et al.* [2012] and figure 1 in *Mitrofanov et al.* [2012] suggests that the same latitude-dependent smoothing of the map has been used in order to suppress noise on smaller scales. *Sanin et al.* [2012] conclude that there are three large permanently shaded regions (PSRs) that contain significant neutron suppressions, while smaller PSRs do not contain significant deviations from the background count rate. No effort is made to compare these measured neutron suppressions, which seem completely in keeping with what one would expect if little of the count rate was actually collimated, with what would be found with the LPNS. As pointed out in section 4.1, a count rate dip above Shoemaker Crater is also very well detected by the LPNS. Thus, no substantive evidence to support claims about the functioning of the collimator in the LEND CSETN can be drawn from the paper by *Sanin et al.* [2012].

4.4. Orbital Phase Profiles

Litvak et al. [2012a] use the orbital phase profile to conclude that the collimated count rate into the LEND CSETN is 1.7 neutrons per second. The orbital phase profile involves averaging over narrow latitude bands either on the near or far side of the Moon. The lengths of these bands are very much greater than the field of view of the collimator, so the purpose of the orbital phase profile is to compare large-scale features in global maps of different energy neutrons in order to determine the fractions of the total LEND CSETN count rate in the lunar collimated and lunar uncollimated components. To achieve this aim, *Litvak et al.* [2012a] assume that the lunar uncollimated component has a variation with longitude and latitude that matches that of the fast neutrons measured by the LEND sensor for high energy neutrons. Not only is this assumption unjustified, but it is also unjustifiable. Monte Carlo neutron transport simulations by *Lawrence et al.* [2011] suggest that high-energy epithermal (HEE) neutrons are the primary contributor to the uncollimated lunar count rate, with a smaller portion from fast neutrons. This is important because, while both HEE and fast neutron fluxes are similarly changed by the increase in mean atomic mass in the mare regions, the HEE neutrons are much more sensitive to hydrogen near the lunar poles. Thus, the assumption made by *Litvak et al.* [2012a] forces the large-scale polar count rate dips to be ascribed to a significant collimated component because the variation of the uncollimated component has been falsely denied the opportunity to contribute to these polar count rate dips. Had the altitude dependence of the count rate variation been simultaneously investigated, then the inappropriateness of this assumption would have been evident.

5. Discussion

The results of the autocorrelation function and power spectrum analyses contained in this paper indisputably show how, even in the polar regions, the maps from the LEND CSETN are lower contrast than those from the LPNS on a range of scales. While much of this is due to the dominant, spatially invariant spacecraft-generated neutron background into the LEND CSETN, the lunar component of the count rate is also seen to display less small-scale power than is found by the LPNS. This deficit of small-scale structure exists to such an extent that the LEND CSETN results are best described by a model where the detector footprint is even slightly broader than omnidirectional for a spacecraft at the 50 km altitude of LRO. The 10 km spatial resolution claimed by some authors [*Mitrofanov et al.*, 2010, 2011, 2012; *Boynton et al.*, 2012] is inconsistent with the LEND CSETN data themselves and thus, once again, this should be rejected as a viable hypothesis. Further, claims that hydrogen enhancements are not colocated with permanently shaded regions [*Mitrofanov et al.*, 2010] and that hydrogen enhancements are present “in both permanently shadowed and illuminated areas” [*Mitrofanov et al.*, 2012] are not supported by the LEND CSETN data.

With just a straightforward scaling argument, one can see why the LPNS produces a more significant map of the count rate variations and hence hydrogen distribution. Suppose that the neutron count rate measured for regolith containing no hydrogen, s_0 , were precisely known for both the LPNS and the LEND CSETN. The ratio of lunar neutron count rate, s , to s_0 sets the local hydrogen abundance. How much longer would the LEND CSETN need to collect data to receive the same accuracy in the derived hydrogen abundance as the LPNS, assuming that they actually have the same sized footprint? If there were not a large spacecraft background contribution to the LEND CSETN, then it would receive just ~ 2 neutrons per second, which is about a tenth of the LPNS rate. Thus, it would need an observation period ten times as long as that of the LPNS to determine s/s_0 to the same fractional precision. However, the uniform spacecraft background contains a comparable variance to that in the lunar signal itself and the background and spacecraft neutrons are not distinguishable for the LEND CSETN. This means that, assuming the mean background count rate were precisely known, an extra factor of two in integration time is required to recover the same fractional accuracy

in the inferred hydrogen abundance. Consequently, for the LEND CSETN to match the hydrogen map from 7 months of the LPNS at an altitude of 30 km would require $t_{LEND} \sim 20 t_{LP} \sim 12$ years. Even then, the LEND CSETN map would be lower in spatial resolution because of the broader instrumental footprint.

At the lower orbital altitude of 30 km, the omnidirectional LPNS map already contains more significant structure than is present in that from the LEND CSETN. Furthermore, the application of image reconstruction techniques has been shown to enhance the contrast in the count rate map by suppressing the inevitable stochastic noise and undoing some of the blurring that is unavoidably associated with the extended detector footprint. This objective assessment makes clear that the most accurate maps of the lunar polar hydrogen distribution are those resulting from LPNS data processed through an image reconstruction algorithm.

The arguments put forward by *Mitrofanov et al.* [2011], *Litvak et al.* [2012a, 2012b], and *Boynton et al.* [2012] in support of the LEND CSETN functioning well as a collimated neutron detector have been considered in the previous section. None of them are found to provide strong evidence to bolster the claims that the majority of the lunar component into the LEND CSETN is collimated. Their conclusions appear to result from a mixture of unjustifiable or demonstrably incorrect assumptions, a misapplication of statistics, or an unrepeatable data reduction process. In contrast, the wide range of measurements considered in detail in this paper are all consistent with the component fractions inferred by *Eke et al.* [2012]; namely that the uniform spacecraft background produces just over half of the counts into the LEND CSETN, with the spatially varying uncollimated lunar background close behind and the collimated lunar component providing fewer than 5% of the total counts.

Collimating epithermal neutrons is distinctly nontrivial and the claims that the LEND CSETN is producing maps with a spatial resolution of 10 km are extraordinary. "In science, the burden of proof falls upon the claimant; and the more extraordinary a claim, the heavier is the burden of proof demanded" [*Truzzi, 1987*]. However, many lines of evidence reject the hypothesis that this level of spatial resolution is achieved. An alternative hypothesis, consistent with the available evidence, was provided by *Eke et al.* [2012]. This hypothesis has passed the further testing performed in this paper, where the different techniques employed have further quantified the footprint of the LEND CSETN. It is likely that plans for future missions to the lunar poles will use maps of the hydrogen distribution, so it is important that the capabilities of the LEND CSETN are properly appreciated in order to prevent costly future mistakes in targeting landers.

Given that the performance of the LEND CSETN instrument has been shown here to be greatly inconsistent with the claims made by various authors, and has not met its primary objective of mapping the lunar neutron flux at a spatial resolution of ~ 10 km, one might reasonably ask how these data can best be used. The detector has, as was pointed out by *Eke et al.* [2012], made the first map of lunar neutrons with this particular energy-dependent filter that is picking out a mixture of high-energy epithermal and fast neutrons. While the map is noisy and suffers from both a large spacecraft background and a very extended spatial footprint, it is still a unique resource. In order to extract scientifically useful results from this instrument, the challenge will be to understand the neutron transport within LRO well enough to determine which energies of neutron is the LEND CSETN measuring, and what they reveal about the composition of the lunar surface.

6. Conclusions

The best available maps of polar hydrogen come from the pixon reconstructions of LP data. These provide estimates of the average weight percentage of water-equivalent hydrogen in polar craters that range up to a few percent and have a fractional uncertainty of $\sim 30\%$ [*Teodoro et al., 2010*]. The LEND CSETN produces maps containing a dominant background from neutrons that arise due to cosmic ray interactions with the spacecraft. The effective detector footprint, taking into account both the collimated lunar and uncollimated background lunar counts may even be broader than that for an omnidirectional detector at 50 km altitude. The suppression in the count rate over Shoemaker Crater is consistent with a statistical fluctuation superimposed upon a broad dip in count rate of the sort that an omnidirectional detector such as the LEND CSETN would measure in this region. Thus, it does not support the claim that the LEND CSETN is collimated.

The results of this study are relevant to the proposed "Fine Resolution" Epithermal Neutron Detector [*Malakhov et al., 2012*] that is scheduled to be launched in 2016 on the ExoMars Trace Gas Orbiter mission.

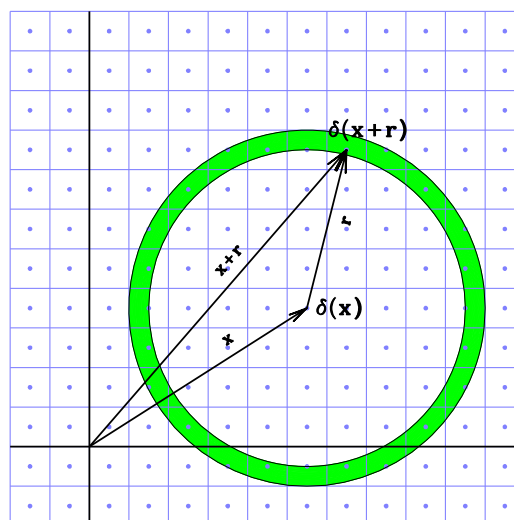


Figure A1. Schematic showing the relevant variables in the autocorrelation function computation: \mathbf{r} and \mathbf{x} .

Appendix A: The Geometry of the Autocorrelation Function

In Figure A1 we present a schematic showing the relevant variables in the autocorrelation function: \mathbf{x} and \mathbf{r} . The overall contribution of the location \mathbf{x} is then given by all the \mathbf{r} vectors within the circle centered at \mathbf{x} with radius $r \equiv |\mathbf{r}|$. The autocorrelation function $\xi(r \equiv |\mathbf{r}|) \equiv \langle \delta(\mathbf{r})\delta(\mathbf{x} + \mathbf{r}) \rangle$, where $\langle \rangle$ denotes *ensemble average*, is computed adding the contribution of all pairs separated by distance r throughout the whole image. This mathematical operation uses the 2-D vector \mathbf{x} as a dummy variable and produces a variable $\xi(r)$ that only depends on the amplitude of \mathbf{r} .

Acknowledgments

L.T. and R.E. acknowledge the support of the NASA Planetary Geology and Geophysics Program Project #07-PGG07-0007 and NASA Planetary Missions Data Analysis Program Project #07-DDAP07-0005 for funding this research. V.R.E. was supported by the STFC rolling grant ST/F002289/1. L.T. acknowledges helpful discussions with J. Karcz.

References

- Adler, R. J. (1981), *The Geometry of Random Fields*, Wiley, Chichester, U. K.
- Arnold, J. R. (1979), Ice in the lunar polar regions, *J. Geophys. Res.*, *84*, 5659–5668.
- Boynton, W. V., et al. (2012), High spatial resolution studies of epithermal neutron emission from the lunar poles: Constraints on hydrogen mobility, *J. Geophys. Res.*, *117*, E00H33, doi:10.1029/2011JE003979.
- Chin, G., et al. (2007), Lunar Reconnaissance Orbiter overview: The instrument suite and mission, *Space Sci. Rev.*, *129*, 391–419, doi:10.1007/s11214-007-9153-y.
- Christensen-Dalsgaard, J., D. Gough, and J. Toomre (1985), Seismology of the sun, *Science*, *229*, 923–931, doi:10.1126/science.229.4717.923.
- Colaprete, A., et al. (2010), Detection of water in the LCROSS ejecta plume, *Science*, *330*, 463–468, doi:10.1126/science.1186986.
- Cole, S., W. J. Percival, J. A. Peacock, and P. Norberg (2005), The 2dF Galaxy Redshift Survey: Power-spectrum analysis of the final data set and cosmological implications, *Mon. Not. R. Astron. Soc.*, *362*, 505–534, doi:10.1111/j.1365-2966.2005.09318.x.
- Eisenstein, D. J., I. Zehavi, D. W. Hogg, R. Scoccimarro, M. R. Blanton, R. C. Nichol, and R. Scranton (2005), Detection of the Baryon Acoustic Peak in the Large-Scale Correlation Function of SDSS Luminous Red Galaxies, *Astrophys. J.*, *633*, 560–574, doi:10.1086/466512.
- Eke, V. (2001), A speedy pixion image reconstruction algorithm, *Mon. Not. R. Astron. Soc.*, *324*, 108–118, doi:10.1046/j.1365-8711.2001.04253.x.
- Eke, V. R., L. F. A. Teodoro, and R. C. Elphic (2009), The spatial distribution of polar hydrogen deposits on the Moon, *Icarus*, *200*, 12–18, doi:10.1016/j.icarus.2008.10.013.
- Eke, V. R., L. F. A. Teodoro, D. J. Lawrence, R. C. Elphic, and W. C. Feldman (2012), A quantitative comparison of lunar orbital neutron data, *Astrophys. J.*, *747*, 6, doi:10.1088/0004-637X/747/1/6.
- Elphic, R. C., D. J. Lawrence, W. C. Feldman, B. L. Barraclough, S. Maurice, A. B. Binder, and P. G. Lucey (1998), Lunar Fe and Ti abundances: Comparison of Lunar Prospector and Clementine data, *Science*, *281*, 1493–1496, doi:10.1126/science.281.5382.1493.
- Elphic, R. C., V. R. Eke, L. F. A. Teodoro, D. J. Lawrence, and D. B. J. Bussey (2007), Models of the distribution and abundance of hydrogen at the lunar south pole, *Geophys. Res. Lett.*, *34*, L13204, doi:10.1029/2007GL029954.
- Feldman, W. C., R. C. Reedy, and D. S. McKay (1991), Lunar neutron leakage fluxes as a function of composition and hydrogen content, *Geophys. Res. Lett.*, *18*, 2157–2160, doi:10.1029/91GL02618.
- Feldman, W. C., B. L. Barraclough, S. Maurice, R. C. Elphic, D. J. Lawrence, D. R. Thomsen, and A. B. Binder (1998a), Major compositional units of the moon: Lunar Prospector thermal and fast neutrons, *Science*, *281*, 1489–1493, doi:10.1126/science.281.5382.1489.
- Feldman, W. C., S. Maurice, A. B. Binder, B. L. Barraclough, R. C. Elphic, and D. J. Lawrence (1998b), Fluxes of fast and epithermal neutrons from Lunar Prospector: Evidence for water ice at the lunar poles, *Science*, *281*, 1496–1500.
- Feldman, W. C., D. J. Lawrence, R. C. Elphic, B. L. Barraclough, S. Maurice, I. Genetay, and A. B. Binder (2000), Polar hydrogen deposits on the Moon, *J. Geophys. Res.*, *105*, 4175–4196, doi:10.1029/1999JE001129.
- Gasnault, O., W. C. Feldman, S. Maurice, I. Genetay, C. d'Uston, T. H. Prettyman, and K. R. Moore (2001), Composition from fast neutrons: Application to the Moon, *Geophys. Res. Lett.*, *28*, 3797–3800, doi:10.1029/2001GL013072.

- Lawrence, D. J., W. C. Feldman, R. C. Elphic, J. J. Hagerty, S. Maurice, G. W. McKinney, and T. H. Prettyman (2006), Improved modeling of Lunar Prospector neutron spectrometer data: Implications for hydrogen deposits at the lunar poles, *J. Geophys. Res.*, *111*, E08001, doi:10.1029/2005JE002637.
- Lawrence, D. J., R. C. Elphic, W. C. Feldman, H. O. Funsten, and T. H. Prettyman (2010), Performance of orbital neutron instruments for spatially resolved hydrogen measurements of airless planetary bodies, *Astrobiology*, *10*, 183–200, doi:10.1089/ast.2009.0401.
- Lawrence, D. J., V. R. Eke, R. C. Elphic, W. C. Feldman, H. O. Funsten, T. H. Prettyman, and L. F. A. Teodoro (2011), Technical comment on “Hydrogen Mapping of the Lunar South Pole Using the LRO Neutron Detector Experiment LEND”, *Science*, *334*, 1058–c, doi:10.1126/science.1203341.
- Lawrence, D. J., et al. (2013), Evidence for water ice Near Mercury’s north pole from MESSENGER neutron spectrometer measurements, *Science*, *339*, 292–296, doi:10.1126/science.1229953.
- Lingenfelter, R. E., E. H. Canfield, and W. N. Hess (1961), The lunar neutron flux, *J. Geophys. Res.*, *66*, 2665–2671, doi:10.1029/JZ066i009p02665.
- Litvak, M. L., I. G. Mitrofanov, A. Sanin, A. Malakhov, W. V. Boynton, G. Chin, and G. Droege (2012a), Global maps of lunar neutron fluxes from the LEND instrument, *J. Geophys. Res.*, *117*, E00H22, doi:10.1029/2011JE003949.
- Litvak, M. L., et al. (2012b), LEND neutron data processing for the mapping of the Moon, *J. Geophys. Res.*, *117*, E00H32, doi:10.1029/2011JE004035.
- Malakhov, A., et al. (2012), Fine Resolution Epithermal Neutron Detector (FRIEND) for ExoMarsTrace Gas Orbiter, in *EGU General Assembly Conference Abstracts*, *EGU General Assembly Conference Abstracts*, vol. 14, edited by A. Abbasi N. Giesen, pp. p. 9118, Copernicus Publisher, Göttingen, Germany.
- Maurice, S., D. J. Lawrence, W. C. Feldman, R. C. Elphic, and O. Gasnault (2004), Reduction of neutron data from Lunar Prospector, *J. Geophys. Res.*, *109*, E07S04, doi:10.1029/2003JE002208.
- McHardy, I. M., E. Koerding, C. Knigge, P. Uttley, and R. P. Fender (2006), Active galactic nuclei as scaled-up galactic black holes, *Nature*, *444*, 730–732, doi:10.1038/nature05389.
- Metzger, A. E., and D. M. Drake (1990), Identification of lunar rock types and search for polar ice by gamma ray spectroscopy, *J. Geophys. Res.*, *95*, 449–460, doi:10.1029/JB095iB01p00449.
- Miller, R. S., G. Nerurkar, and D. J. Lawrence (2012), Enhanced hydrogen at the lunar poles: New insights from the detection of epithermal and fast neutron signatures, *J. Geophys. Res.*, *117*, E11007, doi:10.1029/2012JE004112.
- Mitrofanov, I., W. Boynton, M. Litvak, A. Sanin, and R. Starr (2011), Response to comment on “Hydrogen Mapping of the Lunar South Pole Using the LRO Neutron Detector Experiment LEND”, *Science*, *334*, 1058–d, doi:10.1126/science.1203341.
- Mitrofanov, I., M. Litvak, A. Sanin, A. Malakhov, D. Golovin, W. Boynton, G. Droege, and G. Chin (2012), Testing polar spots of water-rich permafrost on the Moon: LEND observations onboard LRO, *J. Geophys. Res.*, *117*, E00H27, doi:10.1029/2011JE003956.
- Mitrofanov, I. G., A. B. Sanin, D. V. Golovin, M. L. Litvak, A. A. Konovalov, and A. A. Kozyrev (2008), Experiment LEND of the NASA Lunar Reconnaissance Orbiter for high-resolution mapping of neutron emission of the Moon, *Astrobiology*, *8*, 793–804, doi:10.1089/ast.2007.0158.
- Mitrofanov, I. G., A. B. Sanin, W. V. Boynton, G. Chin, J. B. Garvin, D. Golovin, and L. G. Evans (2010), Hydrogen mapping of the lunar south pole using the LRO neutron detector experiment LEND, *Science*, *330*, 483–486, doi:10.1126/science.1185696.
- Monin, A., A. Yaglom, and J. Lumley (2007), *Statistical Fluid Mechanics, Volume 1: Mechanics of Turbulence*, Dover Books on Physics Series, Dover, Mineola, N. Y.
- Narteau, C., D. Zhang, O. Rozier, and P. Claudin (2009), Setting the length and time scales of a cellular automaton dune model from the analysis of superimposed bed forms, *J. Geophys. Res.*, *114*, F03006, doi:10.1029/2008JF001127.
- Neumann, G. A., et al. (2013), Bright and dark polar deposits on Mercury: Evidence for surface volatiles, *Science*, *339*, 296–300, doi:10.1126/science.1229764.
- Paige, D. A., et al. (2013), Thermal stability of volatiles in the north polar region of Mercury, *Science*, *339*, 300–303, doi:10.1126/science.1231106.
- Peebles, P. J. E. (1980), *The Large-Scale Structure of the Universe*, Princeton Univ. Press, Princeton, N. J.
- Pina, R. K., and R. C. Puetter (1993), Bayesian image reconstruction—The pixon and optimal image modeling, *Publ. Astron. Soc. Pac.*, *105*, 630–637.
- Planck Collaboration (2013), Planck 2013 results. XV. CMB power spectra and likelihood. *ArXiv e-prints*.
- Sanin, A. B., I. G. Mitrofanov, M. L. Litvak, A. Malakhov, W. V. Boynton, G. Chin, and G. Droege (2012), Testing lunar permanently shadowed regions for water ice: LEND results from LRO, *J. Geophys. Res.*, *117*, E00H26, doi:10.1029/2011JE003971.
- Teodoro, L. F. A., V. R. Eke, and R. C. Elphic (2010), Spatial distribution of lunar polar hydrogen deposits after KAGUYA (SELENE), *Geophys. Res. Lett.*, *37*, L12201, doi:10.1029/2010GL042889.
- Truzzi, M. (1987), On pseudo-skepticism, *Zetetic Scholar*, *12/13*, 3–4.
- Watson, K., B. Murray, and H. Brown (1961), On the possible presence of ice on the Moon, *J. Geophys. Res.*, *66*, 1598–1600.
- Wieczorek, M. A., and R. J. Phillips (1998), Potential anomalies on a sphere—Applications to the thickness of the lunar crust, *J. Geophys. Res.*, *103*, 1715–1724, doi:10.1029/97JE03136.